Journal of Materials Chemistry A

PAPER

Cite this: J. Mater. Chem. A, 2018, 6, 20093

In situ derived Fe/N/S-codoped carbon nanotubes from ZIF-8 crystals as efficient electrocatalysts for the oxygen reduction reaction and zinc–air batteries†

Huihui Jin,[a] Huang Zhou,[a] Wenqiang Li,[a] Zhihao Wang,[ab] Jinlong Yang,[a] Yuli Xiong,[c] Daping He,*[ab] Lei Chen*[a] and Shichun Mu *[a]

Received 13th August 2018
Accepted 27th September 2018

DOI: 10.1039/c8ta07849a

rsc.li/materials-a

Here we develop for the first time Fe/N/S-codoped carbon nanotubes (Fe/N/S-CNTs), derived from hydrazine hydrate and ferrous sulfate treated metal–organic frameworks, as an efficient ORR catalyst in both alkaline and acidic electrolytes. Hydrazine hydrate serves as a reducing agent to prevent the rapid aggregation of Fe nanocatalysts, which facilitates the growth of CNTs during pyrolysis. And it is discovered for the first time that sulfate ions can be used as a sulfur source to create C–S–C bonds by reaction with carbon at a high temperature. The prepared Fe/N/S-CNTs exhibits excellent ORR activity with a half-wave potential of 0.887 V in alkaline medium, which is 42 mV higher than that of commercial Pt/C (0.845 V), and its half-wave potential is just 26 mV lower than that of Pt/C in acidic medium. In addition, it also has high stability and methanol resistance ability in both alkaline and acidic electrolytes. Furthermore, when used as the cathode in primary Zn–air batteries, the power density of Fe/N/S-CNTs reaches 111 mW cm^{-2}, which is 1.5 times higher than that of Pt/C (73 mW cm^{-2}). Experimental results and DFT calculations demonstrate that the high-yield of CNTs, the optimal balance ratio of pyridinic and graphitic N, and the synergistic effect of C–S–C and Fe–N_x are all essential ingredients for the outstanding ORR performance.

1. Introduction

Sustainable and clean energy conversion technologies (such as fuel cell and metal–air batteries) are urgently desired to replace traditional energy conversion technologies.[1–3] Electrochemical reactions are paramount processes in those devices, especially for the oxygen reduction reaction (ORR), which has a negative influence on most electrochemical devices because of its sluggish kinetics.[4–6] Unfortunately, noble metal catalysts (such as Pt, Pd and their compounds) with high costs and scarce sources are still the most effective ORR catalysts to date, which is responsible for the slow marketization of new energy devices and apparatus.[7–10] Therefore, to realize a widespread use of new energy conversion technologies, an efficient and inexpensive electrocatalyst composed of earth-abundant elements is the ultimate goal and also a tough challenge.

Undoubtedly, various cost-efficient electrocatalysts including carbon nanomaterials,[11,12] transition-metal oxides and hydroxides,[13–15] sulfides,[16,17] and nitrides[18,19] have been developed to improve the ORR kinetics and further reduce the energy consumption of electrochemical processes. Among these advanced materials, carbon nanomaterials have attracted increasing attention due to their unique mechanical, electrical, and chemical properties.[20–22] Especially, carbon nanotubes (CNTs) possess large specific area and high conductivity, presenting strong superiority in electrochemistry.[23] Compared with traditional carbon materials, CNTs have better electron transfer kinetics, excellent anti-poisoning features and corrosion resistance, which are beneficial for catalytic activity and stability.[24] Furthermore, heteroatoms (*e.g.*, transition metal atoms such as Fe, Co, Ni, Mo, *etc.*; non-metal atoms such as N, S, P, B, *etc.*) doped into CNTs can cause electron modulation for preferable electronic and geometric structures, resulting in enhanced electrocatalytic activity.[25,26] Among the various dopants, the combination of Fe and N and the synergistic effect between S and N are highly favorable, which jointly induce excellent ORR activity.[27,28] Hence, CNTs doped with Fe, N and S are a promising candidate as an electrochemical catalyst for various applications in energy conversion.

Recently, metal–organic frameworks (MOFs), a kind of ultrahigh porosity and extremely high surface area crystalline materials, have been extensively developed as various

[a]State Key Laboratory of Advanced Technology for Materials Synthesis and Processing, Wuhan University of Technology, Wuhan 430070, China. E-mail: hedaping@whut.edu.cn; CHL0583@163.com; msc@whut.edu.cn

[b]Hubei Engineering Research Center of RF-Microwave Technology and Application, Wuhan University of Technology, Wuhan 430070, China

[c]School of Electronic and Electrical Engineering, Wuhan Textile University, Wuhan 430200, China

† Electronic supplementary information (ESI) available: Figures and tables. See DOI: 10.1039/c8ta07849a

controllable structure nanomaterial sources for electrochemical devices.[29–31] For example, Lou's group first reported that a single precursor ZIF-67 can be converted into N-doped CNTs with high electrocatalytic activity through pyrolysis in a H_2 atmosphere.[32] Recently, Mai's group developed a general method to prepare CNTs from MOFs *via* a low temperature (as low as 430 °C) and long-time pyrolysis process.[33] Actually, the synthesis of CNTs can be attributed to the catalysis of dispersed metal nanospecies and the low valence state of transition metal ions maintained in the pyrolysis process at low temperature or the presence of H_2. However, long-time pyrolysis increases energy consumption, and the use of H_2 increases risk. Thus, the adoption of a safe, low energy consumption method to prepare high performance catalysts is more conducive to the popularization of catalysts. Our previous work reported that a layer of SiO_2 outside the ZIF-67 nanocrystals can prevent the quick aggregation of Co nanocatalysts, and significantly serves as a unique 'sieve' to induce the catalytic growth of CNTs during pyrolysis.[34]

Herein, we report the direct synthesis of high-yield Fe/N/S-doped CNTs (denoted as Fe/N/S-CNTs) derived from hydrazine hydrate and ferrous sulfate treated ZIF-8 (denoted as H–Fe/ZIF-8). Hydrazine hydrate here performs the function of reducing Fe ions and preventing the quick aggregation of Fe nanoparticles during pyrolysis to promote the formation of CNTs. Surprisingly, S element is found to be included in the pyrolysis product. Since sulfate ion is the only source of S during the synthesis, we speculate that the sulfate ions adsorbed on the surface of H–Fe@ZIF-8 may release SO_2 to react with C and form S at a high temperature, resulting in S doping in the pyrolysis product. The reaction process involves the following equations:

$$SO_4^{2-} \rightarrow SO_2 + SO_3 \quad (1)$$

$$SO_2 + C \rightarrow S + CO_2 \quad (2)$$

The synthesized Fe/N/S-CNTs exhibits excellent ORR performance both in alkaline and acidic solutions. High-angle annular dark field-scanning transmission electron microscopy (HAADF-STEM) mapping coupled with X-ray photoelectron spectroscopy (XPS) confirms the effect of hydrazine hydrate on the morphology and nitrogen state of the product and the result of S doping derived from sulfate. The ORR activity of Fe/N/S-CNTs in terms of the onset and half-wave potential is superior to that of other similar reported materials.

2. Experimental

2.1 Chemicals

All reagents were purchased from Sinopharm Chemical Reagent Co. Ltd. All reagents were analytical grade purity and used without further purification. Commercial Pt/C (20 wt%) was purchased from Shanghai HeSen Electric Co. Ltd. The resistivity of deionized water used in this work was 18.25 MΩ cm.

2.2 Electrocatalyst preparation

$Zn(NO_3)_2 \cdot 6H_2O$ (4.0 mmol) and $FeSO_4 \cdot 7H_2O$ (0.33 mmol) were dissolved in 36 mL of methanol, and then mixed with another 36 mL of methanol with 2-methylimidazole (32.0 mmol) dissolved in it. The mixture was stirred at 35 °C for 6 h and then hydrazine hydrate was added and stirring continued for another 15 h. A creamy yellow precipitate (H–Fe/ZIF-8) was collected and washed with methanol three times by centrifugation and dried at 70 °C in vacuum for 12 h. Other ZIF particles were synthesized using the same method, except for the different amounts of hydrazine hydrate (3 mL, 6 mL, 9 mL, 12 mL, 15 mL and 18 mL), or different iron sources ($FeCl_2 \cdot 4H_2O$). The as-prepared precursors were then pyrolyzed at 900 °C (5 °C min^{-1}) for 3 h in an argon atmosphere. Then the obtained black powders were treated in a mixed solution of hydrochloric acid and DI water ($HCl : H_2O = 1 : 1$) for 24 h to remove the acid soluble by-products. The final products were obtained after washing with DI water several times to neutralize them and by drying at 70 °C overnight. Fe/N/S-CNTs discussed in this paper was prepared using 18 mL hydrazine hydrate. Fe/N/S–C was derived from only $FeSO_4 \cdot 7H_2O$ treated ZIF-8 (Fe/ZIF-8). N–C was derived from ZIF-8. Fe/N/S-CNTs-*x* mL (*x* represents 3, 6, 9, 12 and 15) were derived from different amounts of hydrazine hydrate treated ZIF-8. Fe/N/S-CNTs–$FeCl_2$ was derived from $FeCl_2 \cdot 4H_2O$ and hydrazine hydrate treated ZIF-8.

2.3 Materials characterization

Scanning electron microscopy (SEM) images were acquired on a Zeiss Ultra Plus. Transmission electron microscopy (TEM) and high resolution transmission electron microscopy (HRTEM) images were obtained on a JEM-2100F at 200 kV. Fourier transform infrared (FTIR) spectra were obtained from a Nicolet 6700 FTIR spectrometer. Elemental mapping analysis was conducted on a Titan G2 60-300. X-ray diffraction (XRD) patterns were collected using a D/Max-RB at 12 kW using Cu Kα radiation. Raman spectra were conducted on a Renishaw Invia with an incident laser of 633 nm wavelength. X-ray photoelectron spectroscopy (XPS) measurements were performed on an ESCALAB 250Xi. Elemental compositions were analyzed by Inductively Coupled Plasma-Optical Emission Spectroscopy (ICP-OES) on a Prodigy 7 and ANALYZER (CHNSO) on a Vario EL cube. N_2 adsorption/desorption isotherms and pore size distributions were measured with an ASAP 2020M at 77 K.

2.4 Electrochemical characterization

The electrochemical tests were conducted with a rotating disk electrode (RDE) as the working electrode in 0.1 M KOH and 0.5 M H_2SO_4 on a CHI660E electrochemical workstation using a three-electrode model. Four-electron selectivity was examined with a rotating ring disk electrode (RRDE) on an Autolab PG302N. A platinum wire acted as the counter electrode and an Ag/AgCl electrode filled with saturated potassium chloride was used as the reference electrode in alkaline solution, saturated calomel electrode (SCE) served as the reference electrode in acidic solution, and the measured potentials were converted to a reversible hydrogen electrode (RHE) scale according to the Nernst equation. All the electrochemical tests were performed in N_2/O_2 saturated solution, so N_2/O_2 should be dissolved in the electrolytes for at least 30 minutes to ensure saturation. The

catalyst ink was prepared by sonication of 5 mg as-synthesized catalysts dispersed in 980 μL deionized water/isopropanol (9 : 1) and 20 μL Nafion (5%) solution for 15 minutes. Then 20 μL as-prepared slurry was dropped on the surface of RDE and RRDE, and dried naturally. The commercial Pt/C ink was prepared in a similar way with 3 mg dispersed in the solution, and 10 μL ink was dropped onto the surface of the working electrode. Before use, the working electrode needs to be polished with 0.05 μm alumina slurry. In the RDE testing, CV and LSV plots were recorded at the potential (*vs.* RHE) range of 0–1 V with the scan speed of 5 mV s^{-1} and 1 mV s^{-1}, respectively, in N_2/O_2 saturated solution. In the RRDE testing, the plots were recorded in O_2 saturated solution under the ring potential at 1.5 V *vs.* RHE.

2.5 Zn–air battery tests

Primary Zn–air batteries were fabricated on home-built electrochemical cells. Zinc foil was used as the anode and a 1 cm × 1 cm carbon paper coated with catalyst ink (catalyst loading amount 1.0 mg cm^{-2}) was used as the air cathode. The electrolyte was the mixed solution of 6.0 M KOH and 0.2 M zinc acetate. All the measurements were carried out with a CHI660E electrochemical workstation.

The all solid-state Zn–air battery was composed of a polished zinc foil (anode), nickel mesh loaded with catalysts (cathode), and PVA membrane (solid electrolyte). The PVA membrane was prepared as follows: 1 g PVA powder was added to 45 mL H_2O in which 0.297 g KOH and 0.165 g $Zn(Ac)_2$ were dissolved, and then stirred at 90 °C for at least 30 minutes until the solution transformed into a transparent gel. Then the gel was poured onto a glass plate and freezed in a refrigerator and then dried at 65 °C.

3. Results and discussion

3.1 Morphology and structural characterization

The synthetic process of Fe/N/S-CNTs is shown in Fig. 1a. Fe/N/S-CNTs was derived from H–Fe/ZIF-8, which was simply synthesized by mixing $Zn(NO_3)_2 \cdot 6H_2O$, $FeSO_4 \cdot 7H_2O$, 2-methylimidazole and hydrazine hydrate. N–C (derived from the ZIF-8 precursor without $FeSO_4 \cdot 7H_2O$ and hydrazine hydrate) and Fe/N/S–C (derived from the Fe/ZIF-8 precursor without hydrazine hydrate) were prepared using the same synthetic method as the comparative experiments.

Meanwhile, the amount of hydrazine hydrate added was adjusted, but only the optimal ingredients are discussed here according to primary test results. The morphology of the pyrolysis products was investigated by scanning electron microscopy (SEM) and transmission electron microscopy (TEM). As shown in SEM images (Fig. 1b and ESI, Fig. S1a†), H–Fe@ZIF-8 retains the polyhedral morphology of ZIF-8 with a uniform size of ~50 nm, indicating that the morphology of MOF cannot be destroyed by hydrazine hydrate and iron salts. After a high temperature treatment, Fe/N/S-CNTs has abundant CNTs (Fig. 1c), while Fe/N/S–C has only very few CNTs and N–C retains the polyhedral morphology (ESI, Fig. S1b and c†). In TEM images, Fe/N/S-CNTs shows a large number of CNTs with

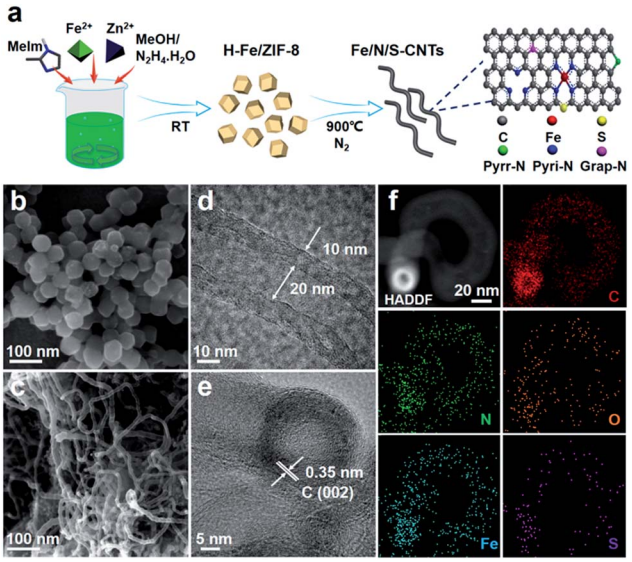

Fig. 1 (a) Schematic synthesis process of Fe/N/S-CNTs; (b) SEM image of H–Fe/ZIF-8; (c) SEM, (d and e) HRTEM images of Fe/N/S-CNTs with (f) HAADF-STEM mapping.

uniform distribution of tube diameter and no obvious large nanoparticles (ESI, Fig. S2a†), but Fe/N/S–C has numerous large size nanoparticles (ESI, Fig. S2b†). High resolution TEM (HRTEM) images further show that the CNTs have an open tube structure with a diameter of 30 nm and a wall thickness of around 10 nm (Fig. 1d and e). The CNT retains the open structure even without acid etching because the catalyst that catalyzes the growth of nanotubes falls off from the top of CNTs (ESI, Fig. S3†), which indicates that the growth of CNTs in this paper occurs in a tip growth mode.[35,36] HAADF-STEM mapping images of Fe/N/S-CNTs show that C, N, O, Fe and S are uniformly distributed along the CNTs (Fig. 1f). Therefore, the addition of hydrazine hydrate during the synthetic process can effectively prevent the iron nanoparticles agglomeration at a high temperature and promote the production of CNTs. In addition, by comparing the Fourier transform infrared spectra (FTIR), it can be found that the infrared spectra of the precursors before pyrolysis (H–Fe/ZIF-8, Fe/ZIF-8) have a vibrational absorption peak of the sulfate ion, which disappears after pyrolysis (Fe/N/S-CNTs and Fe/N/S–C) (ESI, Fig. S4†), proving our conjecture about the possibility of the S doping process.

The structures of the pyrolysis products were detected by X-ray diffraction (XRD) and Raman spectroscopy. The XRD patterns show that the sharp diffraction peaks of Fe/ZIF-8 and H–Fe/ZIF-8 match very well with those of pristine ZIF-8 and the simulated ZIF-8, indicating that the structure of the MOF has no change after the introduction of hydrazine hydrate and iron salts (ESI, Fig. S5a†). After pyrolysis, the sharp diffraction peaks of the MOF disappear giving rise to two typical carbon diffraction peaks located at 26° and 44° indexed to the (002) and (101) planes of carbon, respectively (ESI, Fig. S5b†),[37,38] indicating that the MOF crystals are completely carbonized and partially graphitized with a carbon layer spacing of 0.35 nm as shown in Fig. 1e. Raman spectra of the pyrolysis products further disclose

the characteristic of carbon (ESI, Fig. S6†), D and G bands, corresponding to the peaks at 1300 cm^{-1} and 1580 cm^{-1}, respectively, providing information on the defect degree and graphitization in carbon materials.[39,40] The I_D/I_G ratio of Fe/N/S–C is 1.04 but decreases to 1.00 in Fe/N/S-CNTs due to the generation of more CNTs in Fe/N/S-CNTs, which provide higher conductivity and more electron transport channels to help promote the catalytic activity.

N_2 adsorption/desorption measurement was carried out to investigate the variation in surface area and pore structure of the pyrolysis products. The BET surface areas of Fe/N/S–C and Fe/N/S-CNTs are 498 $m^2\ g^{-1}$ and 611 $m^2\ g^{-1}$, respectively. The adsorption isotherm plots show that the adsorption quantity increases rapidly with the increase of relative pressure, indicating that both micropores and mesopores exist in Fe/N/S-CNTs (Fig. 2a). Pore-size curves disclose that both Fe/N/S-CNTs and Fe/N/S–C have a large number of micropores, and the number of mesopores increases when hydrazine hydrate is introduced, especially the mesopores of 20 nm, due to the open tube structure of CNTs and are consistent with the bore diameter of CNTs (Fig. 2b). Compared to Fe/N/S–C, the increase of mesopores and surface of Fe/N/S-CNTs should be attributed to the formation of CNTs.

The elemental composition and surface chemical state of the pyrolysis products were analyzed by X-ray photoelectron spectroscopy (XPS). From the high-resolution C1s spectra in Fig. 2c, the subpeaks at 284.5 eV and 285 eV represent graphite-like carbon hybridized (sp^2) and diamond-like carbon hybridized (sp^3) features, respectively. Compared to Fe/N/S–C, the C-sp^2 content of Fe/N/S-CNTs shows a noticeable increase, confirming that Fe/N/S-CNTs has more CNTs. The high-resolution N1s spectrum can be subdivided into three different types including graphitic N (grap-N, ~401.8 eV), pyrrolic N (pyrr-N, ~400.1 eV) and pyridinic N (pyri-N, ~398.7 eV).[41,42] It was reported that pyri-N is one of the active sites for the ORR.[43] As shown in Fig. 2d, compared to Fe/N/S–C, the proportion of pyri-N in Fe/N/S-CNTs is enhanced greatly, which not only ensures the high limited current density, but also provides more active sites. The high-resolution Fe2p spectra can be fitted into six peaks from 708 eV to 725 eV (Fig. 2e), namely Fe/Fe_3C (708 eV), $Fe2p_{3/2}$ (Fe(II), Fe(III) 711–713 eV), satellite peak (718.7 eV) and $Fe2p_{1/2}$ (Fe(II), Fe(III) 725.2 eV), demonstrating that both Fe(III) and Fe(II) exist in Fe/N/S–C and Fe/N/S-CNTs.[10] However, the content of Fe/Fe_3C in Fe/N/S–C is much more than that in Fe/N/S-CNTs, indicating that Fe atoms in Fe/N/S–C aggregate into metallic Fe or Fe_3C more easily, resulting in less Fe–N_x active sites. In addition, in the peak table of XPS spectra (ESI, Table S1†), Fe atoms on the surface of Fe/N/S–C (0.51%) and Fe/N/S-CNTs (0.59%) have similar atomic percent, while the N atomic percent in the surface of Fe/N/S-CNTs (6.21%) is more than twice of Fe/N/S–C (3.01%), indicating more Fe–N_x active sites in the surface of Fe/N/S-CNTs. The high-resolution S2p spectrum of Fe/N/S-CNTs displays two kinds of S peaks, including thiophene-S (C–S–C, 163.9 eV and 165 eV) and oxidized-S (SO_x–C, 167.8 eV) (Fig. 2f), where C–S–C has been determined as an active site of the ORR.[6] Furthermore, through the Elemental Analyzer (CHNSO) and Inductively Coupled Plasma-Optical Emission Spectroscopy (ICP-OES) test, the content of S was found to be up to 1% in Fe/N/S-CNTs (ESI, Table S1†), indicating that S atoms can be effectively doped into the pyrolysis product in the present strategy.

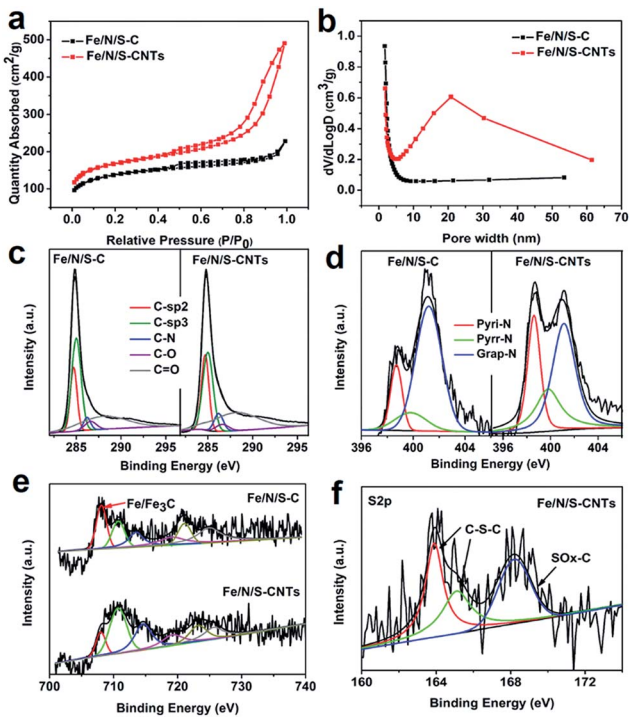

Fig. 2 (a) N_2 sorption isotherms and (b) pore-size distribution of Fe/N/S–C and Fe/N/S-CNTs; (c) C1s XPS spectra of Fe/N/S–C and Fe/N/S-CNTs; (d) N1s XPS spectra of Fe/N/S–C and Fe/N/S-CNTs; (e) Fe2p XPS spectra of Fe/N/S–C and Fe/N/S-CNTs; (f) S2p XPS spectrum of Fe/N/S-CNTs.

3.2 Electrochemical performance

The ORR performance was firstly examined in 0.1 M KOH medium on the rotating disk electrode (RDE). As shown in Fig. S7 (ESI),† cyclic voltammetry (CV) plots show that Fe/N/S-CNTs exhibits obvious ORR activity corresponding to the oxygen reduction absorption peak in O_2-saturated solution. Linear sweep voltammetry (LSV) plots show that the onset potential of Fe/N/S-CNTs (0.987 V) is 20 mV higher than that of commercial Pt/C (0.967 V), and the half-wave potential ($E_{1/2}$) of Fe/N/S-CNTs (0.887 V) is 42 mV higher than that of Pt/C (0.845 V) (Fig. 3a), illustrating that Fe/N/S-CNTs has remarkable ORR activity in alkaline medium. In addition, the rotating ring disk electrode (RRDE) was further studied to identify the electron-transfer mechanism (Fig. 3b). The disk current test results on RRDE are consistent with the results on RDE, demonstrating the reliability of ORR test results. Notably, Fe/N/S-CNTs (0.005 mA) has a lower ring current than Pt/C (0.01 mA) exhibiting a lower H_2O_2% yield, and the electron transfer number (n) of Fe/N/S-CNTs is calculated to be ~4. Additionally, the Koutecky–Levich (K–L) equation was used to calculate electron transfer number based on the LSV plots with different

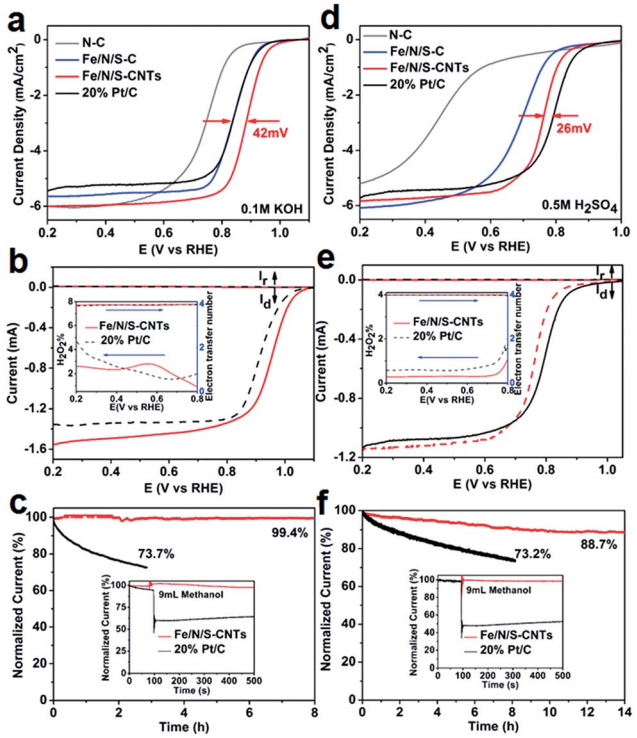

Fig. 3 (a) LSV curves of N–C, Fe/N/S–C, Fe/N/S-CNTs and 20% Pt/C in O_2 saturated 0.1 M KOH electrolyte at 1600 rpm; (b) RRDE test of the ORR on Fe/N/S-CNTs and 20% Pt/C in O_2 saturated 0.1 M KOH (inset: peroxide yield and electron transfer number of Fe/N/S-CNTs and 20% Pt/C); (c) chronoamperometric responses of Fe/N/S-CNTs and 20% Pt/C in O_2 saturated 0.1 M KOH (inset: chronoamperometric responses of Fe/N/S-CNTs and 20% Pt/C catalysts with methanol injection); (d) LSV curves of N–C, Fe/N/S–C, Fe/N/S-CNTs and 20% Pt/C in O_2-saturated 0.5 M H_2SO_4 electrolyte at 1600 rpm; (e) RRDE test of the ORR on Fe/N/S-CNTs and 20% Pt/C in O_2-saturated 0.5 M H_2SO_4 (inset: peroxide yield and electron transfer number of Fe/N/S-CNTs and 20% Pt/C); (f) chronoamperometric responses of Fe/N/S-CNTs and 20% Pt/C in O_2-saturated 0.5 M H_2SO_4 (inset: chronoamperometric responses of Fe/N/S-CNTs and 20% Pt/C catalysts with methanol injection).

rotating speeds (ESI, Fig. S8†), the slopes of the fitting curves show that n is close to 4. The Tafel slope of Fe/N/S-CNTs, N–C, Fe/N/S–C, and Pt/C are 73 mV dec^{-1}, 110 mV dec^{-1}, 78 mV dec^{-1}, and 77 mV dec^{-1}, respectively (ESI, Fig. S9†). The lowest Tafel slope of Fe/N/S-CNTs proves that Fe/N/S-CNTs shows the best ORR activity. Furthermore, Fe/N/S-CNTs exhibits better stability than Pt/C, as the normalized current of Fe/N/S-CNTs decreases less than 1% after 8 h testing, while it fades by 30% after 3 h in Pt/C. In the methanol-resistant test, the normalized current of Fe/N/S-CNTs remains unchanged after methanol injection, while it decreases rapidly in Pt/C, indicating that Fe/N/S-CNTs has excellent methanol resistance (Fig. 3c).

To further demonstrate the positive effect of hydrazine hydrate on the CNT transformation and ORR activities of the obtained products, Fe/N/S-CNTs-x mL (x represents 3 mL, 6 mL, 9 mL, 12 mL, and 15 mL) was prepared by the addition of different amounts of hydrazine hydrate. It can be found that even with the addition of a small amount of hydrazine hydrate, the growth of CNTs will increase (ESI, Fig. S10†), and the proportion of pyri-N will also increase (ESI, Fig. S11†). Their ORR activities are shown in Fig. S12 (ESI),† their onset potentials and half-wave potentials increase with increase in the amount of hydrazine hydrate at first, which stop increasing when the added hydrazine hydrate is sufficient to react with the iron ions. In order to further realize the ORR active sites of Fe/N/S-CNTs, several comparative experiments were carried out. In previous research studies, it has been found that metal nanoparticles, metal oxides, metal sulfides, metal nitrides and metal carbides can all catalyze oxygen reduction. However, it is difficult to know whether these substances are synergistic or independent, and which one has the best catalytic activity. In this paper, the ORR activities of Fe/N/S-CNTs before and after acidic treatments and SCN-poisoning were compared. Fe/N/S-CNTs without acid etching will retain several superficial acid soluble by-products including iron oxides, sulfides and carbides, which are confirmed by the XRD result in Fig. S13 (ESI).† The ORR activity of Fe/N/S-CNTs after acid etching is better than that of Fe/N/S-CNTs before acid etching due to the fact that more Fe–N_x active sites are exposed after acid treatment, but after further poisoning surface Fe–N_x active sites with 0.01 M KSCN, the ORR activity of Fe/N/S-CNTs is greatly reduced (ESI, Fig. S14†). Therefore, to some extent, the contribution of Fe–N_x to the ORR is higher than those of acid soluble by-products. To prove that S doping caused by sulfate ions is favorable for the ORR activity, ferrous sulfate was replaced by ferrous chloride to prepare a catalyst without S for comparison. LSV plots show that the ORR activity (both the onset potential and half-wave potential) of the catalyst with S doping is better than that of the catalyst without S (ESI, Fig. S15†).

Since Fe/N/S-CNTs displays excellent ORR performance under alkaline conditions, it is worth exploring its performance under acidic conditions. The CV curves show that Fe/N/S-CNTs possesses obvious ORR activity in acidic medium (ESI, Fig. S16†). Fig. 3d shows that the half-wave potential of Fe/N/S-CNTs is 0.767 V, which is only 26 mV lower than that of commercial Pt/C (0.793 V), but much better than most of the previously reported non-precious metal electrocatalysts (ESI, Table S2†). In addition, the RRDE test in Fig. 3e shows that the ring current of Fe/N/S-CNTs is 0.00075 mA, which is almost half that of Pt/C (0.0013 mA). And the H_2O_2% yield of Fe/N/S-CNTs is calculated to be lower than that of Pt/C at the full oxygen reduction potential range, the electron transfer number is calculated to be ~4 in accordance with the good fitting of K–L plots (ESI, Fig. S17†). Moreover, in the stability and methanol resistance test, the normalized current of Fe/N/S-CNTs only drops 11.7% after 14 h testing, and remains constant after methanol injection, while the normalized current of Pt/C drops 26.8% after 8 h testing and decreases immediately after methanol injection, indicating that Fe/N/S-CNTs also has better stability and methanol resistance than Pt/C in acidic medium (Fig. 3f).

3.3 DFT calculation and performance of Zn–air batteries

To explain the positive synergistic effect of C–S–C and Fe–N_x for the ORR, density functional theory (DFT) studies were

performed based on the two theoretical model structures in Fig. 4a and b. According to the model structures, the ΔE_{O_2} on Fe/N/S-CNTs (3.4 eV) is much higher than that of Fe/N-doped carbon nanotubes (Fe/N-CNTs) (1.50 eV), indicating that oxygen molecules are more easily adsorbed onto Fe/N/S-CNTs. The enhanced O_2 adsorption energy is beneficial to increase the coverage of O_2 on the catalyst, which accelerates the process of oxygen reduction and makes the catalyst exhibit outstanding oxygen reduction performance.[7,9] Additionally, the density of states (DOS) of carbon-based catalysts is also an effective index to predict the ORR activity.[17] As shown in Fig. 4c, the calculated total DOS of Fe/N/S-CNTs exhibits higher states in the characteristic low-DOS region near the Fermi level compared to Fe/N-CNTs, verifying with the above results that O_2 can be readily adsorbed onto Fe/N/S-CNTs to exhibit better ORR performance, which is consistent with the experimental results. These results directly demonstrate that the synergy between the C–S–C bond and Fe–N_x is more effective and favorable for the ORR.

Considering that Fe/N/S-CNTs has the advantages of being cost-efficient, easy synthesis and outstanding performance in both alkaline and acidic media, it may be a promising candidate for practical application. Here, a primary Zn–air battery is fabricated based on Fe/N/S-CNTs as the air cathode (Fig. 4d). The Fe/N/S-CNTs-based Zn–air battery shows an open-circuit potential of 1.49 V, only slightly higher than that of commercial Pt/C (1.46 V) (ESI, Fig. S18†), but in the polarization and power density curves (Fig. 4e), Fe/N/S-CNTs displays a peak power density of 111 mW cm^{-2}, far exceeding that of Pt/C (73 mW cm^{-2}). Fig. 4f shows the results of discharge measurements at 5 mA cm^{-2} and 20 mA cm^{-2}. Fe/N/S-CNTs exhibits a stable discharge platform of 1.35 V and 1.23 V at 5 mA cm^{-2} and 20 mA cm^{-2}, respectively, which are higher than that of Pt/C (1.22 V at 5 mA cm^{-2}, 1.08 V at 20 mA cm^{-2}). Moreover, Fe/N/S-CNTs still shows a high open circuit voltage of 1.35 V in the all-solid-state Zn–air battery, and can light up a ~3.4 V LED with three all-solid-state Zn–air batteries interconnected in series (Fig. 4g).

Therefore, the brilliant ORR performances of Fe/N/S-CNTs in both alkaline and acidic media can be attributed to the following factors: firstly, CNTs in Fe/N/S-CNTs not only provide electron transport channels but also enhance the conductivity of catalysts; secondly, the active sites of C–S–C and Fe–N_x coordinate with each other to boost the ORR activity; finally, the high specific surface area promotes more effective contact between reactants and catalyst active sites.

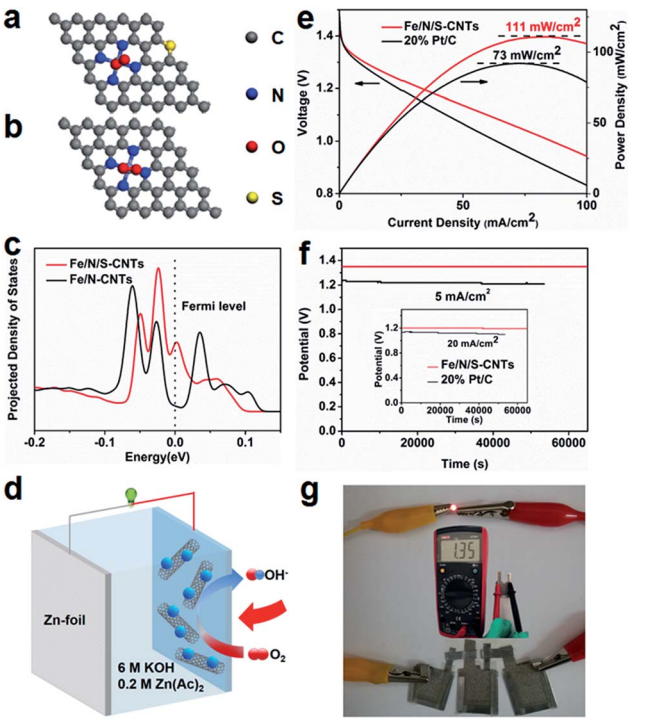

Fig. 4 Model configurations of monolayer N-doped graphene analogue particles with and without S, (a) Fe/N/S-CNTs, (b) Fe/N-CNTs; (c) density of states of Fe/N/S-CNTs and Fe/N-CNTs; (d) schematic diagram of the primary Zn–air battery; (e) polarization and power density curves of Fe/N/S-CNTs and 20% Pt/C; (f) discharge curves of Fe/N/S-CNTs and 20% Pt/C at 5 mA cm^{-2} and 20 mA cm^{-2} current densities; (g) photographs of a lighted LED (~3.4 V) powered by three all-solid-state Zn–air batteries interconnected in series and an open-circuit voltage of 1.35 V.

4. Conclusions

In summary, we successfully prepared Fe/N/S-CNTs *via* direct pyrolysis of hydrazine hydrate and ferrous sulfate treated ZIF-8, in which hydrazine hydrate can effectively prevent the aggregation of iron nanoparticles and promote the large production of CNTs, and sulfate ions provide the source of S enabling S doping of the product at a high temperature. DFT calculations showed that S doping had a significant effect on the promotion of ORR activity for Fe/N/S-CNTs. The prepared Fe/N/S-CNTs exhibited excellent ORR activity, superior stability and methanol tolerance in both alkaline and acidic media. The primary Zn–air batteries based on the electrocatalyst possessed high peak power density, and a stable discharge platform. This research for the first time reports hydrazine hydrate treatments on a metal–organic framework to promote the formation of carbon nanotubes, and proposes that sulfate ions can facilitate doping of carbon materials with S at a high temperature, which opens up a new strategy for the synthesis of carbon nanotubes and S doping.

Conflicts of interest

There are no conflicts to declare.

Acknowledgements

This work was supported by the National Natural Science Foundation of China (51701146, 51672204).

Notes and references

1 K. Ai, Y. Liu, C. Ruan, L. Lu and G. Lu, *Adv. Mater.*, 2013, **25**, 998–1003.
2 B. Weng, C. Grice, W. Meng, L. Guan, F. Xu, Y. Yu, C. Wang, D. Zhao and Y. Yan, *ACS Energy Lett.*, 2018, **3**, 1434–1442.

3 X. M. Xu, C. Su, W. Zhou, Y. L. Zhu, Y. B. Chen and Z. P. Shao, *Adv. Sci.*, 2016, **3**, 500187.
4 Y. P. Wu, W. Zhou, J. Zhao, W. W. Dong, Y. Q. Lan, D. S. Li, C. Sun and X. Bu, *Angew. Chem., Int. Ed.*, 2017, **56**, 13001–13005.
5 D. P. He, Y. L. Xiong, J. L. Yang, X. Chen, Z. X. Deng, M. Pan, Y. D. Li and S. C. Mu, *J. Mater. Chem. A*, 2017, **5**, 1930–1934.
6 H. Shen, E. Gracia-Espino, J. Ma, K. Zang, J. Luo, L. Wang, S. Gao, X. Mamat, G. Hu, T. Wagberg and S. Guo, *Angew. Chem., Int. Ed.*, 2017, **56**, 13800–13804.
7 W. Chen, J. Kim, S. Sun and S. Chen, *Phys. Chem. Chem. Phys.*, 2006, **8**, 2779–2786.
8 D. S. He, D. He, J. Wang, Y. Lin, P. Yin, X. Hong, Y. Wu and Y. Li, *J. Am. Chem. Soc.*, 2016, **138**, 1494.
9 Y. Wang, K. B. Yin, J. Zhang, C. H. Si, X. T. Chen, L. F. Lv, W. S. Ma, H. Gao and Z. H. Zhang, *J. Mater. Chem. A*, 2016, **4**, 14657–14668.
10 Y. Zuo, D. Rao, S. Li, T. Li, G. Zhu, S. Chen, L. Song, Y. Chai and H. Han, *Adv. Mater.*, 2018, **30**, 1704171.
11 L. Ma, S. Chen, Z. Pei, Y. Huang, G. Liang, F. Mo, Q. Yang, J. Su, Y. Gao, J. Zapien and C. Zhi, *ACS Nano*, 2018, **12**, 1949–1958.
12 S. Yang, L. Zhi, K. Tang, X. Feng, J. Maier and K. Müllen, *Adv. Funct. Mater.*, 2012, **22**, 3634–3640.
13 L. Wei, H. E. Karahan, S. Zhai, H. Liu, X. Chen, Z. Zhou, Y. Lei, Z. Liu and Y. Chen, *Adv. Mater.*, 2017, **29**, 1701410.
14 Z. S. Wu, S. Yang, Y. Sun, K. Parvez, X. Feng and K. Müllen, *J. Am. Chem. Soc.*, 2012, **134**, 9082–9085.
15 X. Lv, W. Lv, W. Wei, X. Zheng, C. Zhang, L. Zhi and Q. H. Yang, *Chem. Commun.*, 2015, **51**, 3911–3914.
16 S. J. Rowley-Neale, J. M. Fearn, D. A. Brownson, G. C. Smith, X. Ji and C. E. Banks, *Nanoscale*, 2016, **8**, 14767–14777.
17 I. S. Amiinu, Z. H. Pu, X. B. Liu, K. A. Owusu, H. G. R. Monestel, F. O. Boakye, H. N. Zhang and S. C. Mu, *Adv. Funct. Mater.*, 2017, **27**, 1702300.
18 C. Bezerra, L. Zhang, K. Lee, H. Liu, A. Marques, E. Marques, H. Wang and J. Zhang, *Electrochim. Acta*, 2008, **53**, 4937–4951.
19 S. H. Ahn, X. Yu and A. Manthiram, *Adv. Mater.*, 2017, **29**, 606534.
20 I. S. Amiinu, J. Zhang, Z. K. Kou, X. B. Liu, O. K. Asare, H. Zhou, K. Cheng, H. N. Zhang, L. Q. Mai, M. Pan and S. C. Mu, *ACS Appl. Mater. Interfaces*, 2016, **8**, 29408–29418.
21 X. Cao, C. Tan, M. Sindoro and H. Zhang, *Chem. Soc. Rev.*, 2017, **46**, 2660.
22 F. He, G. Chen, Y. S. Zhou, Y. G. Yu, L. Q. Li and S. Hao, *J. Mater. Chem. A*, 2016, **4**, 3822–3827.
23 W. Yang, X. Liu, X. Yue, J. Jia and S. Guo, *J. Am. Chem. Soc.*, 2015, **137**, 1436.
24 S. P. P. Su, H. Xiao, J. Zhao, Y. Yao, Z. G. Shao, C. Li and Q. H. Yang, *Chem. Sci.*, 2013, **4**, 2941–2946.
25 J. H. Kim, Y. J. Sa, Y. J. Hu and H. J. Sang, *ACS Appl. Mater. Interfaces*, 2017, **9**, 9567.
26 Q. Lin, X. Bu, A. Kong, C. Mao, F. Bu and P. Feng, *Adv. Mater.*, 2015, **27**, 3431.
27 D. H. Kwak, S. B. Han, Y. W. Lee, H. K. Park, I. A. Choi, K. B. Ma, M. C. Kim, S. J. Kim, D. H. Kim, J. I. Sohn and K. W. Park, *Appl. Catal., B*, 2016, **203**, 889–898.
28 Q. Shi, F. Peng, S. Liao, H. Wang, H. Yu, Z. Liu, B. Zhang and D. Su, *J. Mater. Chem. A*, 2013, **1**, 14853–14857.
29 L. Tao, C. Y. Lin, S. Dou, S. Feng, D. W. Chen, D. D. Liu, J. Huo, Z. H. Xia and S. Y. Wang, *Nano Energy*, 2017, **41**, 417–425.
30 J. Duan, S. Chen and C. Zhao, *Nat. Commun.*, 2017, **8**, 15341.
31 J. Ying, J. Li, G. Jiang, Z. Cano, Z. Ma, C. Zhong, D. Su and Z. Chen, *Appl. Catal., B*, 2018, **225**, 496–503.
32 B. Xia, Y. Yan, N. Li, H. B. Wu, X. W. Lou and X. Wang, *Nat. Energy*, 2016, **1**, 15006.
33 J. S. Meng, C. J. Niu, L. H. Xu, J. T. Li, X. Liu, X. P. Wang, Y. Z. Wu, X. M. Xu, W. Y. Chen, Q. Li, Z. Z. Zhu, D. Y. Zhao and L. Q. Mai, *J. Am. Chem. Soc.*, 2017, **139**, 8212–8221.
34 H. Zhou, D. P. He, I. S. Amiinu, J. L. Yang, Z. Wang, J. Zhang, Q. R. Liang, S. Yuan, J. W. Zhu and S. C. Mu, *Nanoscale*, 2018, **10**, 6147–6154.
35 Y. H. Mo, A. K. M. F. Kibria and K. S. Nahm, *Synth. Met.*, 2001, **122**, 443–447.
36 S. Amelinckx, X. B. Zhang, D. Bernaerts, X. F. Zhang, V. Ivanov and J. B. Nagy, *Science*, 1994, **265**, 635–639.
37 G. Jia, W. Zhang, G. Fan, Z. Li, D. Fu, W. Hao, C. Yuan and Z. Zou, *Angew. Chem., Int. Ed.*, 2017, **56**, 13781–13785.
38 W. J. Jiang, L. Gu, L. Li, Y. Zhang, X. Zhang, L. J. Zhang, J. Q. Wang, J. S. Hu, Z. Wei and L. J. Wan, *J. Am. Chem. Soc.*, 2016, **138**, 3570.
39 J. Zhang, H. Zhou, X. B. Liu, J. Zhang, T. Peng, J. L. Yang, Y. H. Huang and S. C. Mu, *J. Mater. Chem. A*, 2016, **4**, 15870–15879.
40 H. Zhang, S. Hwang, M. Wang, Z. Feng, S. Karakalos, L. Luo, Z. Qiao, X. Xie, C. Wang, D. Su, Y. Shao and G. Wu, *J. Am. Chem. Soc.*, 2017, **139**, 14143.
41 B. Ni, C. Ouyang, X. Xu, J. Zhuang and X. Wang, *Adv. Mater.*, 2017, 1701354.
42 B. You, N. Jiang, M. L. Sheng, W. S. Drisdell, J. K. Yano and Y. J. Sun, *ACS Catal.*, 2015, **5**, 7068–7076.
43 Q. C. Wang, Y. P. Lei, Z. Y. Chen, N. Wu, Y. B. Wang, B. Wang and Y. D. Wang, *J. Mater. Chem. A*, 2018, **6**, 516–526.